*remote sensing*

MDPI

*Article*

# Responses of Satellite Chlorophyll-a to the Extreme Sea Surface Temperatures over the Arabian and Omani Gulf

**Manal Hamdeno [1,2], Hazem Nagy [1,3,*], Omneya Ibrahim [1] and Bayoumy Mohamed [1,4]**

[1] Oceanography Department, Faculty of Science, Alexandria University, Alexandria 21500, Egypt
[2] Freshwater and Oceanic Science Unit of Research (FOCUS), University of Liège, 4000 Liège, Belgium
[3] Marine Institute, Rinville, H91 R673 Galway, Ireland
[4] Department of Arctic Geophysics, University Centre in Svalbard, 9171 Longyearbyen, Norway
* Correspondence: hazem.nagy@marine.ie

**Abstract:** Extreme events such as Marine Heat Waves (MHWs) and Low Chlorophyll-a (LChl-a) in the ocean have devastating impacts on the marine environment, particularly when they occur simultaneously (i.e., the compound of MHWs and LChl-a events). In this study, we investigate the spatiotemporal variability of MHWs and LChl-a events in the Arabian and Omani Gulf. For this purpose, we used satellite-based high-resolution observations of SST (0.05° × 0.05°; from 1982 to 2020) and chlorophyll-a concentration data (0.04° × 0.04°; from 1998 to 2020). Hourly air temperature, wind, and heat flux components from the European Centre for Medium-Range Weather Forecasts (ECMWF) reanalysis (ERA5) were used to explain the link between these extreme events and atmospheric forcings. Moreover, our results revealed that the annual frequency of MHW and LChl-a is related to the El Niño-Southern Oscillation (ENSO) and the Indian Ocean Dipole (IOD). The results revealed an average SST warming trend of about 0.44 ± 0.06 °C/decade and 0.32 ± 0.04 °C/decade for the Arabian Gulf (AG) and the Gulf of Oman (OG), respectively. This warming rate was accompanied by MHW frequency and duration trends of 0.97 events/decade and 2.3 days/decade, respectively, for the entire study region from 1982 to 2020. The highest annual MHW frequencies were recorded in 2010 (6 events) and 2020 (5 events) associated with LChl-a frequency values of 4 and 2, respectively. La Niña events in 1999, 2010, 2011, and 2020 were associated with higher frequencies of MHW and LChl-a. The positive phase of IOD coincides with high MHW frequency in 2018 and 2019. The longest compound MHW and LChl-a event with a duration of 42 days was recorded in 2020 at OG. This extreme compound event was associated with wind stress reduction. Our results provide initial insights into the spatiotemporal variability of the compound MHW and LChl-a events that occurred in the AG and OG.

**Keywords:** Arabian Gulf; Gulf of Oman; marine heat waves; chlorophyll-a; extreme compound events; ENSO



**Citation:** Hamdeno, M.; Nagy, H.; Ibrahim, O.; Mohamed, B. Responses of Satellite Chlorophyll-a to the Extreme Sea Surface Temperatures over the Arabian and Omani Gulf. *Remote Sens.* **2022**, *14*, 4653. https://doi.org/10.3390/rs14184653

Academic Editors: Hainan Gong, Peng Zhang and Luca Lelli

Received: 4 August 2022
Accepted: 14 September 2022
Published: 17 September 2022



## 1. Introduction

Marine heat waves (MHWs) are becoming more intense and frequent as a result of global warming [1,2] and have been observed in the world's oceans and regional seas [3–6]. These extreme MHW events have ecological and socioeconomic impacts, including coral bleaching [7], mortality of benthic communities [8], blooms of harmful algae [9], low chlorophyll-a concentrations [10,11], loss of seagrass, mangroves, and kelp forests [12–14], and alteration of fish communities [15]. The most recent definition of MHW is "an anomalous warm water event of at least five days duration with a sea surface temperature (SST) above the 90th percentile climatology" [16]. Numerous studies around the world have examined the factors that influence individual MHW events. For example, a combination of local oceanic and large-scale atmospheric influences was proposed as the cause of the 2010/2011 marine heat wave off the coast of Western Australia, which caused catastrophic

damage to local algal populations and coral bleaching on local reefs [12–14]. Another example of MHWs occurred in the northeastern Pacific Ocean in 2014–2016 [10,17,18], characterized by an anomalous SST of more than 3 °C above the climatological threshold, and classified as an extreme MHW according to the [19] MHW categorization scale. In recent decades, MHWs have been observed in many marginal seas around the world, such as in the Mediterranean Sea (e.g., [4,20–23]), the Tasman Sea in 2015/2016 [24], the Red Sea (e.g., [5,25]), Black Sea [6], and even in the Arctic region (e.g., the Barents sea) [26]. Recently, [27] studied the drivers and trends of MHWs in the Indian Ocean from 1982 to 2018 and their role in modulating the Indian monsoon. They found that accelerated warming in the Indian Ocean plays a crucial role in increasing the frequency of MHWs. They also found that the El Nino has a major impact on MHWs during the summer monsoon. Moreover, Ref. [28] studied the characteristics of MHWs in the Arabian Sea from 1982 to 2019 and found that the frequency of MHWs increased by about 1.5–2 events/decade and attributed this accelerated trend to the increase in mean SST.

The strategic location of the Arabian Gulf (AG) and the Omani Gulf (OG) is highlighted by their connection to the oil, gas, and fishing industries [29–31]. AG acts as a shipping hub connecting European ports to China and East Asia via the Strait of Hormuz [32]. The AG is considered one of the most vulnerable marine ecosystems [30,31], and is characterized by extremely high temperatures and salinity [33,34]. One of the most well-known phenomena in the OG is the upwelling system (see Figure 1), which is driven by the southwest monsoon winds [35,36]. This upwelling brings cold and nutrient-rich water to the surface [36,37], increasing surface productivity [35–37]. Low Chlorophyll-a (LChl-a) events can threaten marine ecosystems that rely on phytoplankton as the basis of their food web [38]. So, the combination of the two extreme events (i.e., MHW and LChl-a) could have catastrophic consequences for marine life. The AG and OG have rich ecosystems, therefore studying the coincidence of MHWs and LChl-a events in this region is critical for the conservation of these natural habitats. Compound MHW and LChl-a events are defined when both extremely high temperatures and low chlorophyll-a conditions coincide in time and space [11]. The interaction of several extreme events often leads to major climate-related catastrophes [11,39]. These compound events can have significant impacts on marine ecosystems, such as reduced nutrients and low productivity, which can threaten marine life that relies on phytoplankton as the foundation of its food web [38]. These compound events have been documented on a global scale [11,40–42]. However, there are no previous studies on this topic in AG and OG.

In the satellite era, extensive research has been conducted to study the SST [33,43–46] and chlorophyll-a concentration [47–49] in AG and OG. For example, Ref. [43] found a strong relationship between sea level pressure, meridian wind, and air temperature with SST over AG and OG from 2001 to 2015, indicating the important role of atmospheric circulation in SST variability in this region. A significant SST trend ($0.6 \pm 0.3$ °C/decade) was observed by [44] in AG between 2002 and 2018, with the highest values in Kuwait Bay and north AG. Alosairi et al. [45] noted an extreme SST in Kuwait Bay on 31 July 2020, accompanied by an atmospheric heat wave and an extended period of Kous winds (an Arabic word for northwesterly winds) characterized by high humidity and accompanied by large-scale intermittent fish kills along the entire Kuwait coast. In addition, Ref. [46] analyzed the daily SST from 2003 to 2019 in AG and OG. They mentioned that the trends of SST and 95th percentiles are about 0.08 °C/year and 0.07 °C/year, respectively. Recently, Ref. [33] found that the SST trend in AG from 1982–2020 was about $0.41 \pm 0.14$ °C/decade. The study concluded that the SST variability is related to the large-scale atmospheric changes caused by the El Nino-Southern (ENSO), Atlantic Multi-decadal Oscillation (AMO), and Indian Ocean Dipole (IOD) climate modes. The seasonal and interannual variability of Chl-a concentration was studied by [47] over the period (1997–2006). They found that the seasonal variability of Chl-a in AG was related to SST, runoff, and wind stress. In contrast, this variability in OG was associated with summer upwelling events caused by strong seasonal monsoon winds. In addition, high Chl-a concentrations in the northwestern and

central parts of AG were found to coincide with a decrease in the wind stress and an increase in SST in late summer and fall. Nezlin et al. [48] investigated the influence of meteorological parameters (e.g., wind and precipitation) on the variability of phytoplankton in AG between 1997 and 2009. The highest surface productivity was noticed in the northwestern part of the Gulf, which was influenced by the Shatt Al-Arab runoff. The maximum Chl-a concentration was observed in winter while the minimum was in spring/summer. Their results revealed that the Chl-a interannual variability in the southern part of AG was associated with precipitation rather than wind and SST. They also found a phytoplankton bloom in the southern AG from 2000 to 2008 that coincided with low precipitation. Moradi and Kabiri [49] investigated the spatio-temporal variability of SST and Chl-a in AG from 2002 to 2013. The highest Chl-a concentrations were observed in coastal areas with an average of 0.1 to 0.5 mg.m$^{-3}$. The study concluded that, the seasonal variability of Chl-a in the central and northwestern regions of the AG was related to river discharge, water circulation, and climate regimes. Hussein et al. [50] studied the relationship between SST and Chl-a, and their relationship with bathymetry in the UAE coasts from 2003 to 2019, and concluded that the highest positive correlation between chlorophyll-a and SST was found in the shallow coastal areas and vice versa in the deep waters. They also mentioned that the highest Chl-a concentration was observed in the Strait of Hormuz.

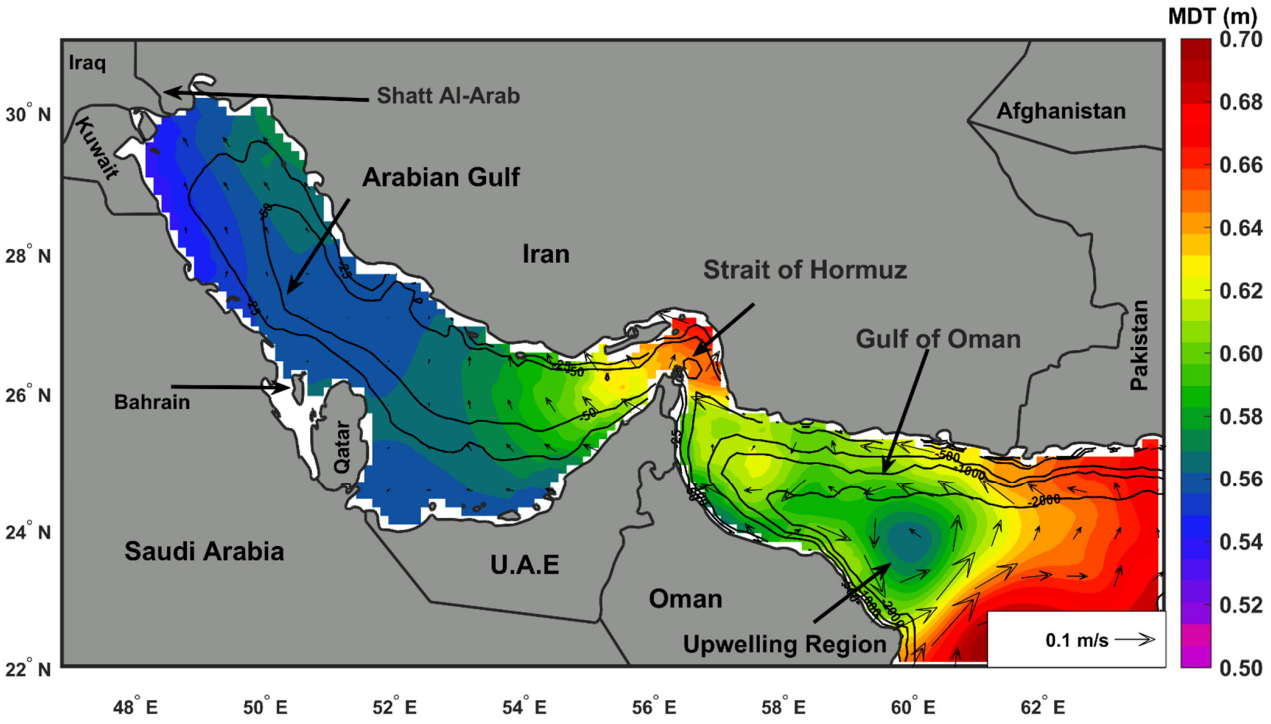


**Figure 1.** The mean dynamic topography (MDT) from 1993–2012 (shading, in meters) and general geostrophic circulation (black arrows, in m/sec) of the Arabian and Oman Gulfs were obtained from (MDT Global CNES-CLS18: Aviso+ (altimetry.fr); accessed on 30 April 2022), with the main geographic features (e.g., countries and rivers). Isobaths of 25, 50, 500, 1000, and 2000 m are shown as white contours obtained from the General Bathymetric Chart of the Oceans (GEBCO) (www.gebco.net; accessed on 15 April 2022).

Recently, there have been some attempts to study MHWs in the Indian Ocean, including the Arabian Gulf [27,28]. However, these studies have not included LChl-a events associated with MHWs in their investigations. To fill this gap, we used the high-resolution SST and Chl-a data from the remote sensing satellites to investigate the link between the MHWs and LChl-a. We then investigated the spatiotemporal variability of the main MHW characteristics in the Arabian Gulf and the Gulf of Oman. In addition, we investigate the possible relationship between atmospheric forcings (air temperature, net heat flux, and

wind stress) during the longest compound event that occurred in our do-main during the study period. Finally, we examine the modulation of their frequency by large-scale climate mode variability (e.g., ENSO and IOD).

## 2. Materials and Methods

### *2.1. The Study Area*

The AG is a semi-enclosed marginal sea extending 251,000 km from the Strait of Hormuz in the south to Shatt-Al-Arab in the north [29,51]. In the northeastern part of the AG, small river inputs (mainly from the Euphrates and Tigris rivers) are dominant [51]. The AG is a shallow evaporative basin with a depth rarely exceeding 50 m (i.e., the Gulf is on average 35 m deep [48], connected to the much deeper OG (>2000 m) via the Strait of Hormuz [52], see Figure 1). The Mean Dynamic Topography (MDT) with a horizontal resolution of $1/8^\circ \times 1/8^\circ$ from 1993–2012, obtained from Archiving, Validation, and Interpretation of Satellite Oceanographic data (AVISO; MDT Global CNES-CLS18: Aviso+ (altimetry.fr), [53,54]; accessed on 30 April 2022), is used to plot the general circulation in the study area (Figure 1). The monsoon winds affecting our study region are the northeast monsoon (from November to February, with surface winds over OG, blowing predominantly from the northeast [55]) and the southwest monsoon (from June to mid-September, with surface winds over the region blowing predominantly from the southwest [56]). The southwest monsoon is stronger than the northeast monsoon [57]. During the southwest monsoon, coastal upwelling occurs along the coast of Oman, with the effect being stronger in the southern part of the coast [58]. The circulation is dominated by a permanent cyclonic eddy in the OG [59,60], which is associated with coastal upwelling in this region [36,37]. This upwelling system consists of nearshore upwelling that extends to about 750 km off the coast of Oman [36] and can also be observed in the Gulf of Oman (cyclonic eddy activity, see Figure 1). The prevailing wind direction in the northern AG, the northwest wind (i.e., Shamal wind) dominates throughout the year [61], sometimes interrupted by southeasterly Kous wind in winter [62]. The topography of the region (e.g., the Zagros Mountains along the Iranian coast) also plays an important role in strengthening the wind [63]. The Shamal wind is capable of producing violent sand and dust storms [61].

### *2.2. Datasets*

In this study, we used the daily high-resolution SST data obtained from the Copernicus Marine Environment Monitoring Service website (CMEMS; https://resources.marine.copernicus.eu/?option=com_csw&view=details&prouct_id=SST_GLO_SST_L4_REP_OBSERVATIONS_010_011; downloaded on 22 February 2022). The product name is "SST GLO SST L4 REP OBSERVATIONS 010 011". The CMEMS Operational SST and Ice Analysis (OSTIA) reprocessed analysis product is based on an SST satellite and in-situ observation [64]. The SST dataset consists of daily gap-free maps of SST and ice concentration (referred to as the L4 product) with a horizontal grid resolution of $0.05^\circ \times 0.05^\circ$ [65]. The Arabian Gulf CMEMS OSTIA data were extracted from the global data, resulting in a regularly grided dataset of 61,721 points covering 14,245 days from 1 January 1982 to 31 December 2020.

Daily Chl-a concentration data are obtained from CMEMS (Data | Copernicus Marine; downloaded on 15 March 2022). The product is based on the merging of data derived from the sensors SeaWiFS, MODIS, MERIS, VIIRS-SNPP&JPSS1, OLCI-S3A&S3B. The data set has a spatial resolution of $0.04^\circ \times 0.04^\circ$ and a daily temporal resolution. Chl-a data for AG and OG were extracted from the global data, resulting in a regularly gridded dataset of 88,753 points covering 8401 days from 1 January 1998 to 31 December 2020.

The atmospheric data are obtained from the European Centre for Medium-Range Weather Forecasts (ECMWF) ERA5 [66] (https://cds.climate.copernicus.eu/cdsapp#!/dataset/reanalysis-era5-single-levels (downloaded on 20 April 2022; from 1982 to 2020). The dataset has a spatial resolution of $0.25^\circ \times 0.25^\circ$ and hourly time step. The atmospheric fields used are the wind components at 10 m altitude (U10 and V10), air temperature at 2 m altitude (T2m), shortwave surface net radiation ($Q_s$), longwave surface net radiation

($Q_b$), sensible surface heat flux ($Q_h$), and latent surface heat flux ($Q_e$). Daily averages were calculated by averaging the hourly ERA5 data for the same period from 1982 to 2020.

Finally, the normalized monthly oceanic El Niño-Southern Oscillation (ENSO) time series for the aforementioned period was obtained from National Oceanic and Atmospheric Administration (NOAA) [67] (https://psl.noaa.gov/data/climateindices/list/; accessed 28 August 2022). The Indian Ocean Dipole (IOD) was downloaded from Japan Agency for Marine-Earth Science and Technology (JAMSTEC) (https://www.jamstec.go.jp/virtualearth/general/en/; accessed 28 August 2022). NOAA identifies El Niño (warm) and La Niña (cool) events in the tropical Pacific. It is the three-month average of the SST anomaly for the El Niño 3.4 region (i.e., 5°N–5°S, 120°–170°W). Events are defined as five consecutive, overlapping three-month periods with an anomaly of +0.5 °C or above for warm (El Niño) events and with an anomaly of −0.5 °C or below for cold (La Niña) events. According to [68], the IOD is defined as the SST anomaly difference between the West Pole off East Africa (50°E–70°E, 10°S–10°N) and the East Pole off Sumatra (90°E–110°E, 10°S-Eq).

### *2.3. Methods of Analysis*

In this work, we use the standard MHW approach of [16], that allows the identification of MHWs throughout the year, not only during the summer months, which are critical for various biological applications [26]. This definition is as follows: "an unusually warm water event lasting at least five or more consecutive days with SST above the seasonally fluctuating threshold of 90th percentile for that time of year". We used the MATLAB toolbox M_MHW [69] to detect all the MHWs metrics (frequency, duration, intensity) and the LChl-a events. The MATLAB toolbox M_MHW can be freely downloaded at the website https://github.com/ZijieZhaoMMHW/m_mhw1.0; accessed 20 March 2022. Here, we ran the MHW code twice, the first run was based on the climatological baseline from 1982 to 2020 and the second was based on the overlapping period between SST and Chl-a data (1998–2020). The overlapping period was used to compare the occurrence of MHWs associated with LChl-a events. We also used the same MATLAB toolbox to detect the lowest 10th percentile of the Chl-a dataset, which represents the LChl-a events. Each MHW event is described by a set of metrics [16,19], as follows: duration (in days) is "the time between the start and end dates of an event", frequency (in events) is "the number of events that occurred each year", mean intensity (°C) is "the average sea surface temperature anomaly (SSTA) over the duration of the event", and maximum intensity (°C) is "the highest SSTA during an event". The SST and Chl-a anomalies were deduced relative to the daily climatology.

Linear trends in SSTA, and MHW characteristics are estimated using Theil–Sen estimates [70] rather than ordinary least squares estimates which could be biased due to non-normally distributed data and the presence of outliers [1]. The statistical significance of these trends is determined using the Modified Mann–Kendall (MMK) test at a 95% confidence level [71,72].

We used ERA5 datasets to estimate the mean and anomalies of air temperature and the surface net heat flux $Q_T$ ($W/m^2$) during the longest compound event in 2020 (from 10 July 10 to 21 August 2020). The mean surface net heat flux is calculated according to [73] and described in [74,75] as follows:

$$Q_T = Q_s + Q_b + Q_e + Q_h$$

where $Q_b$ and $Q_s$ represent the radiation terms [76], while $Q_h$ and $Q_e$ represent the turbulence terms [77]. The word radiation refers to the transfer of heat from the sun to the ocean ($Q_s$), which is the primary source of energy for the global ocean. Longwave infrared radiation $Q_b$ returns some of the absorbed solar energy to the atmosphere, but some of this radiation is scattered by clouds and atmospheric moisture and returns to the ocean. Cloud cover has the greatest influence on the radiation terms ($Q_b$ and $Q_s$), while specific humidity and air and sea surface temperature have less influence on their variations [78–80]. The

turbulent terms ($Q_h$ and $Q_e$) are influenced by specific humidity, the difference between air and sea surface temperature, and wind speed [81,82].

The zonal and meridional wind stress components ($\tau_{wx}$, $\tau_{wy}$) were calculated according to [83] in ($N/m^2$),

$$\tau_{(x,y)} = C_D\ \rho_a\ |W_{(x,y)}| * W_{(x,y)}$$

where $\rho_a$ is the air density = 1.2 ($kg/m^3$), the $C_D$ is a constant drag coefficient ($1.25 \times 10^{-3}$) which is used to estimate the wind stress components according to [84], and W is referred to as the components of the wind speed (m/s). Daily mean values of atmospheric parameters were obtained by averaging hourly data, and the daily anomaly of air temperature, wind stress, and net heat flux was calculated by subtracting the historical mean (1982–2020) from the mean during the compound event (from 10 July to 21 August 2020) at each grid point. In addition, we investigated the role of two climate indices (ENSO and IOD) on the modulation of MHW/LChl-a frequencies.

## 3. Results

### *3.1. Sea Surface Temperature Climatology, and Trend (1982–2020)*

Figure 2a shows the spatial distribution of SST climatology for our domain over the study period (1982–2020). The average SST climatology ranged from 23 to 28 °C across the study region. The lowest values (<24 °C) of SST climatology are observed in the northern part of AG off the Kuwaiti and Iraqi coasts, while the highest values (>28 °C) are found in the northern part of OG off the Omani coast. Figure 2b shows a map of the spatial SST trend map for the entire study area from 1982 to 2020. A statistically significant trend ($p < 0.05$) is detected across the whole AG and OG basins. The linear trend in the AG ranged from 0.4 to 0.65 °C/decade with an average of 0.44 °C/decade, while the SST trend in the OG was lower, varying from 0.15 to 0.45 °C/decade with an average of 0.32 °C/decade. The highest significant warming trend values (>0.6 °C/decade) are found in the northern part of AG off the Saudi and Iranian coasts. The lowest significant trend values (<0.3 °C/decade) are observed along the southern part of the Omani coast.

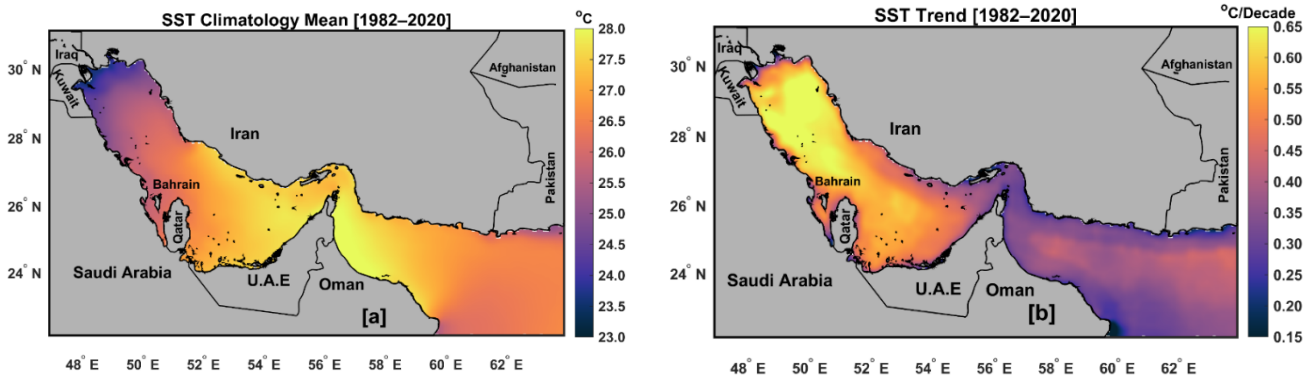


**Figure 2.** The spatial maps of mean SST in °C (**a**) and the trend of deseasonalized SST in °C/decade (**b**) from 1982 to 2020.

The temporal evolution of monthly SSTA across AG and OG from 1982 to 2020 is shown in Figure 3a,b. The average SSTA warming trend was about 0.44 ± 0.06 °C/decade and 0.32 ± 0.04 °C/decade for AG and OG, respectively. The highest anomalies are observed in both gulfs in 2010 and 2020, while the lowest values are in 1984 and 1991/1992. Negative SST anomalies predominate from 1982 to 1991, while positive SST anomalies predominate after 1992. In general, the spatial and temporal trends of AG are higher than those of OG.

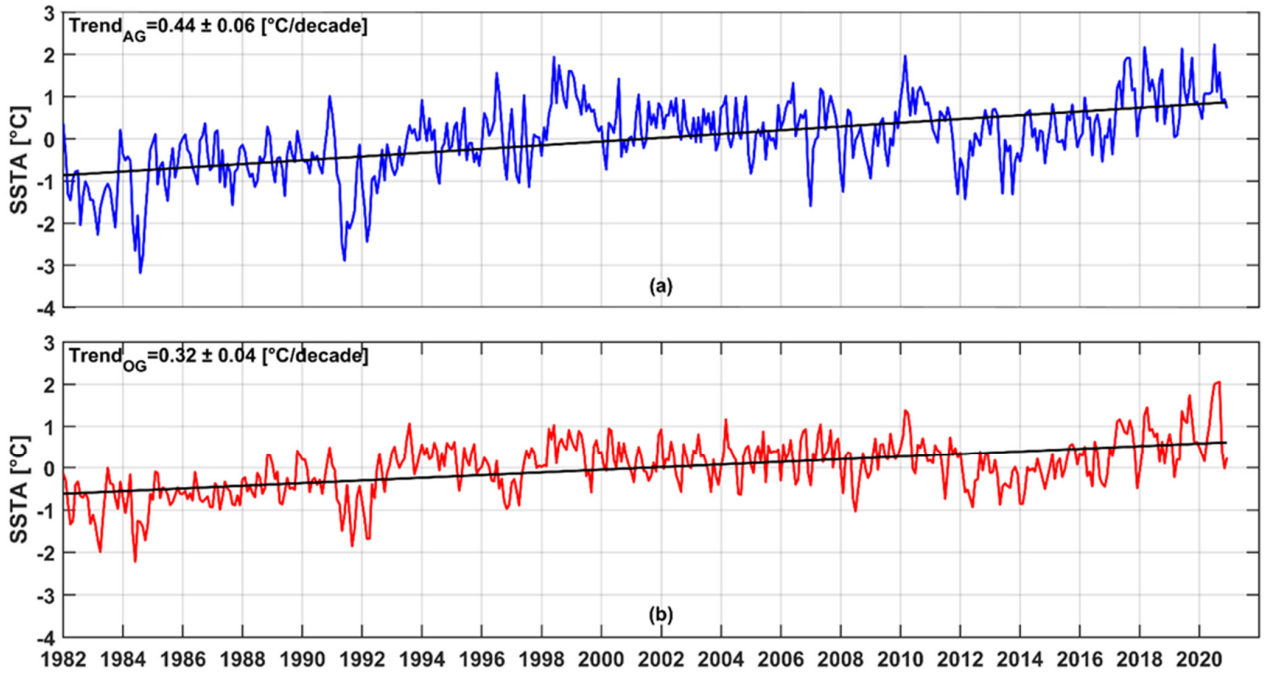


**Figure 3.** The temporal evolution of the monthly averaged SSTA for AG (**a**) and OG (**b**) from 1982 to 2020. The SSTA trend is shown by the solid black line.

### *3.2. The Inter-Annual Variability of the MHW Characteristics (1982–2020)*

The temporal variability of the main annual MHW metrics (frequency and duration) and their relationship with the annual mean SST for AG and OG throughout the study period are shown in Figure 4a–d. For both gulfs, the highest annual MHW frequencies are observed in 1998, 1999, 2010, and in the last four years of the study period (i.e., 2017–2020) with more than four events/year. The lowest MHW frequencies in both gulfs are observed from 1982 to 1992 and from 2012 to 2014 with less than one event/year. These years are considered cold years (see Figure 4a,b), with the lowest SSTA variability as already noted by [33]. We also found an interesting MHW frequency peak (~7 events/year) at AG in 2010. This peak could be related to the high SSTAs (~ 2 °C) in that year (Figure 3a) and to the strong cold phase of the ENSO (La Niña) that occurred in 2010. This positive ENSO phase was associated with a high SST, as already mentioned in [85,86].

In AG and OG, the annual MHW duration varied between 5 and 35 days/year from 1982 to 2020 (Figure 4b). In AG, the longest annual MHW duration (>20 days/year) is recorded in 2017, 2018, and 2019, while the shortest MHW duration (~5 days/year) is observed in 1987 and 1992. For OG, the highest MHW duration (>20 days/year) is recorded in 2020, and the lowest (~5 days/year) in 1984. The trend in annual MHW frequency increased significantly ($p < 0.05$) throughout the study period with a value of 0.95 events/decade and 0.97 events/decade for AG and OG, respectively. For the whole region, this trend was 0.97 events/decade. The trend in annual MHW duration was not significant for either region ($p > 0.05$), with an average of 2.3 days/decade for the entire study area.

Annual mean SST and MHW metrics (frequency and duration) are highly correlated ($p < 0.05$) across AG and OG at 95% confidence interval (Figure 4c,d). A strong relationship is found between SST and MHW frequency, with correlation coefficients of 0.84 and 0.88 for AG and OG, respectively. For MHW duration, these correlations are 0.71 and 0.63 respectively.

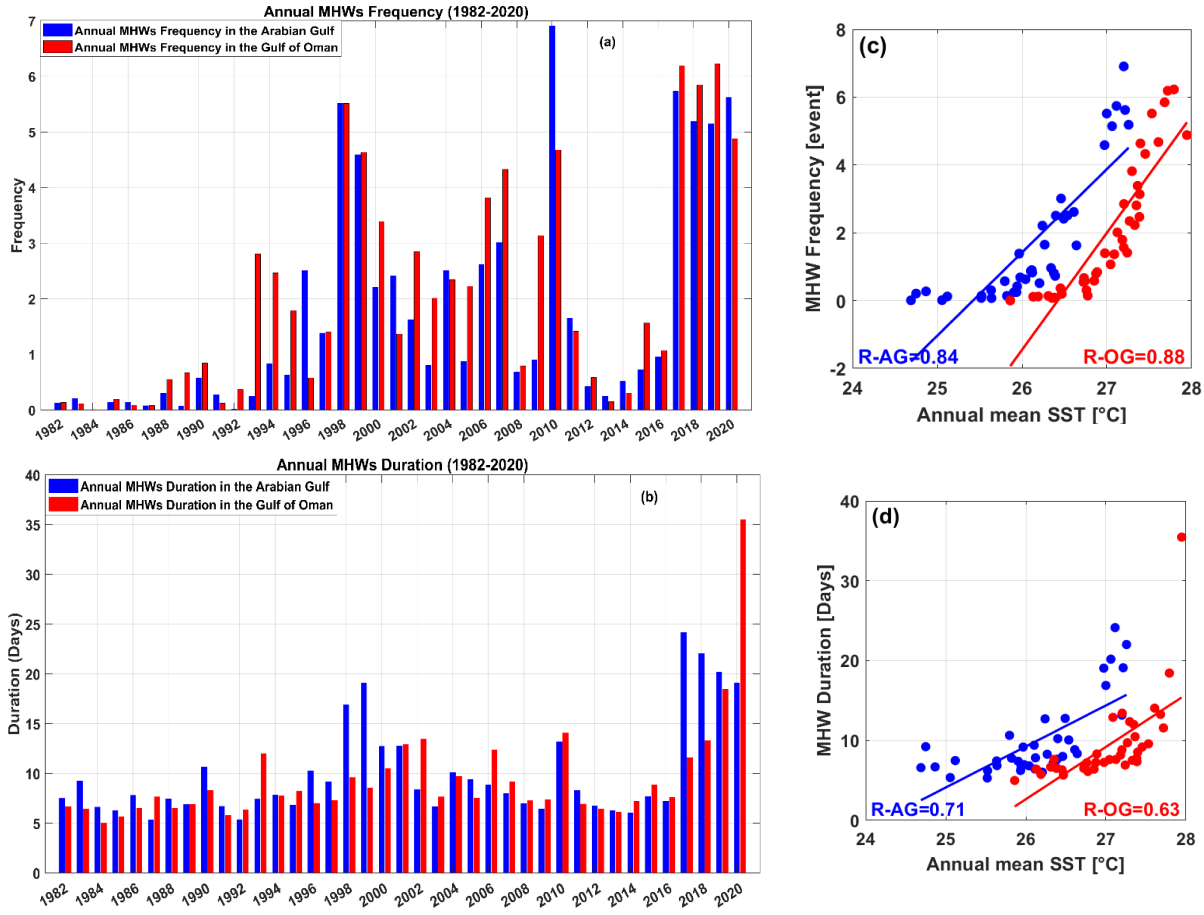


**Figure 4.** Regionally averaged annual means of the MHW (**a**) frequency (events/year), and (**b**) Duration (days/year). The blue and red bars represent the Arabian and Oman Gulfs (AG and OG), respectively. The right panels show the scatter plots of annual mean SST versus annual mean MHW (**c**) frequency, and (**d**) duration over the AG (blue) and OG (red) from 1982 to 2020, with the blue and red lines representing the best-fit linear curve.

### *3.3. Mean and Trends of MHW Characteristics (1982–2020)*

Figure 5a–d depicts the spatial distribution of the annual mean and trend of frequency and duration of MHW from 1982 to 2020. The pattern of mean MHW frequency shows high spatial variability from AG to OG (Figure 5a). The mean annual MHW frequency varies from 1 to 2.5 events, with the highest values observed in the basin of OG (i.e., mainly on the Omani coast), while the lowest mean annual frequency is observed in the northern part of AG and the southeastern part of OG (off Pakistani coast). The mean annual duration of MHWs ranged from less than 10 days in the Strait of Hormuz and the northern part of OG to more than 15 days in the northwestern part of AG (Figure 5b). In general, the AG is characterized by long-lasting and less frequent annual MHWs, whereas annual MHWs at the OG are characterized by high frequency and short duration (Figure 5a,b).

A statistically significant ($p < 0.05$) MHW frequency trend is observed across the study area. The highest annual MHW frequency trend (up to 1.5 events/decade) is detected in the northern part of OG (Figure 5c). The maximum and most significant annual MHW duration trend (>6 days/decade) was found in the northwestern part of AG (i.e., the same regions that showed the highest SST trend; see Figure 2b) and the southeastern part of OG (Figure 5d). The other regions showed a non-significant ($p > 0.05$) trend in annual MHW duration.

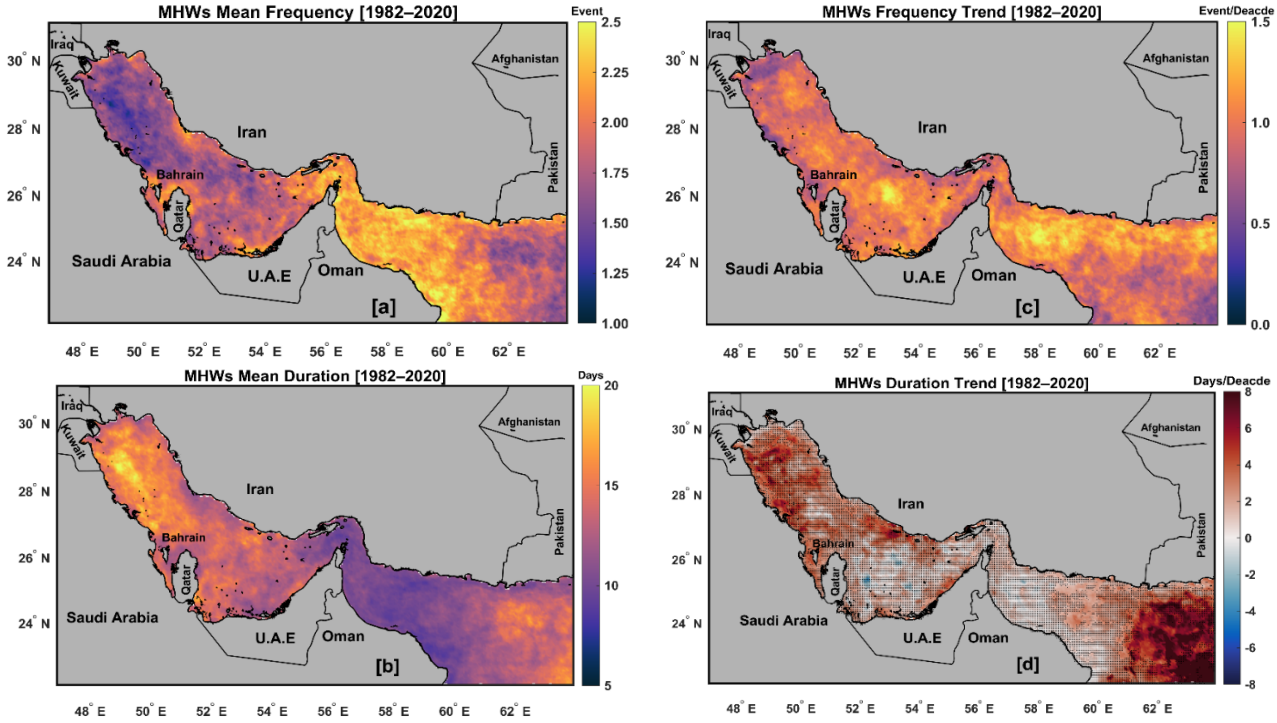


**Figure 5.** The spatial distribution of the annual MHW (**a**) mean frequency (events), (**b**) mean duration (days), (**c**) frequency trend (events/decade), and (**d**) duration trend (days/decade) from 1982 to 2020. Dotted regions show that the trend is statistically insignificant at the 95% confidence interval ($p > 0.05$).

### *3.4. Compound Relation between LChl-a and MHW Events (1998–2020)*

The temporal variability of SST and Chl-a concentration anomalies for AG and OG from 1998 to 2020 is shown in Figure 6. For both basins, the highest temporal Chl-a anomaly is observed in December 2008, which is consistent with [49] who found the reason for this increase is related to the red tide. High Chl-a concentration is also observed between December 2018 and January 2019 in both gulfs (Figure 6a,b). The coincidence between the high SST and low Chl-a concentration anomalies in both gulfs is noticed in 1999, 2010, 2018, 2019, and 2020. In general, the occurrence of low Chl-a anomalies became more frequent in the last decade (2010–2020).

The compound between MHWs and LChl-a events is often defined when they occur simultaneously [11]. Figures 7 and 8 show the spatial distribution of mean intensity and duration of MHW and LChl-a events and their correlation maps from 1998 to 2020. The LChl-a intensity ranges from $-1$ to 0 mg/m$^3$, with the largest negative anomaly of Chl-a concentration ($<-0.75$ mg/m$^3$) found in the coastal areas of OG, in the northernmost part of AG (Shatt-Al-Arab region), and off the southeastern coast of Bahrain. At the same time, these areas also have a high mean MHW intensity (>1.5 °C; Figure 7b) and the highest correlation (>0.6; Figure 7c). This coincidence between the highest negative Chl-a anomaly and intense MHWs in these three regions could be a good example of compound extreme events.


**Figure 6.** Time series anomalies of SST (red line) and Chl-a concentration (green line) for (**a**) the Arabian Gulf and (**b**) the Gulf of Oman between 1998 and 2020.

The spatial distribution of MHW and LChl-a durations is shown in Figure 8a,b. The longest MHWs (>14 days) occur in the northwestern part of AG and the southern part of OG (Figure 8a). The longest LChl-a events (>13 days) occur in the southern part of OG and the northern part of AG (Figure 8b). The spatial correlation between the duration of MHW and LChl-a (Figure 8c) showed a very high correlation (>0.7) between the areas with long MHW and long LChl-a. Particularly for the southeastern part of OG, which will be discussed in more detail in Section 3.6.

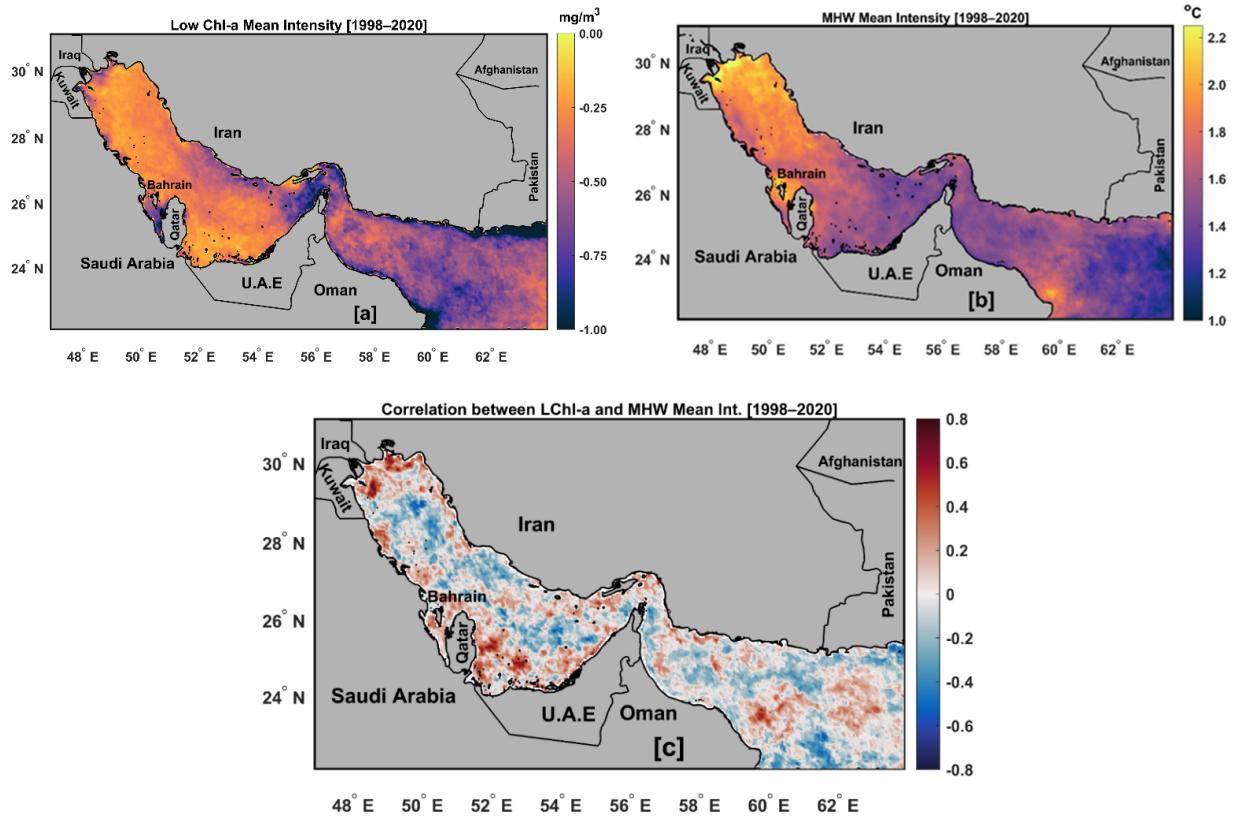


**Figure 7.** The spatial distribution of (**a**) LChl-a mean intensity (mg/m$^3$), (**b**) MHW mean intensity (°C), and (**c**) the spatial correlation map between them from 1998 to 2020 over the entire region.

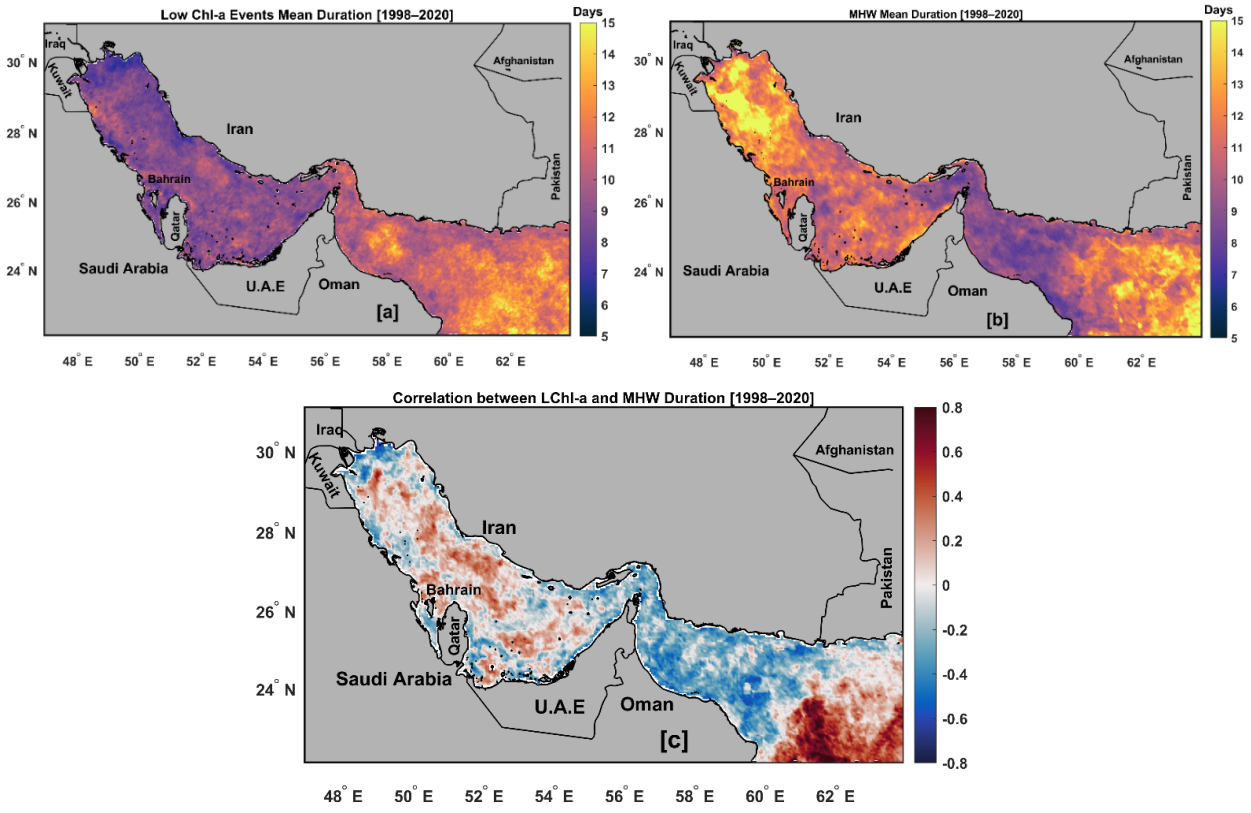


**Figure 8.** The spatial distribution of (**a**) LChl-a mean duration (days), (**b**) MHW mean duration (days), and (**c**) the spatial correlation map between them from 1998 to 2020 over the entire region.

### *3.5. Relationship between MHW/LChl-a and Climate Indices*

Here we examine the possible relationship between climate indices (ENSO and IOD) and the annual frequency of MHW and LChl-a for the entire study area. Oceanic La Niña conditions exist when ENSO is $\leq -0.5$. While El Niño phase occurs when ENSO values are $\geq +0.5$. A positive IOD period is characterized by warmer than average water in the tropical western Indian Ocean. Conversely, a negative IOD period is characterized by cooler than average water in the same region. A large number of MHW events between 1982 and 2020 were associated with La Niña throughout the study area (i.e., 1999, 2000, 2007, 2010, and 2011) (Figure 9a). For example, more than five MHW events were observed during the strongest La Niña events in 1999 and 2010. A high number of LChl-a events between 1998 and 2020 were associated with La Niña in 1999, 2008, 2010, and 2011. Furthermore, a high number of MHW and LChl-a events coincided with the negative phase of ENSO (La Niña) in 1999, 2010, 2011, and 2020. MHW and LChl-a events in 1998 and 2010 were associated with the negative phase of IOD. On the other hand, more than five MHW events were observed to coincide with a strong positive phase of IOD in 2018 and 2019 (Figure 9b).

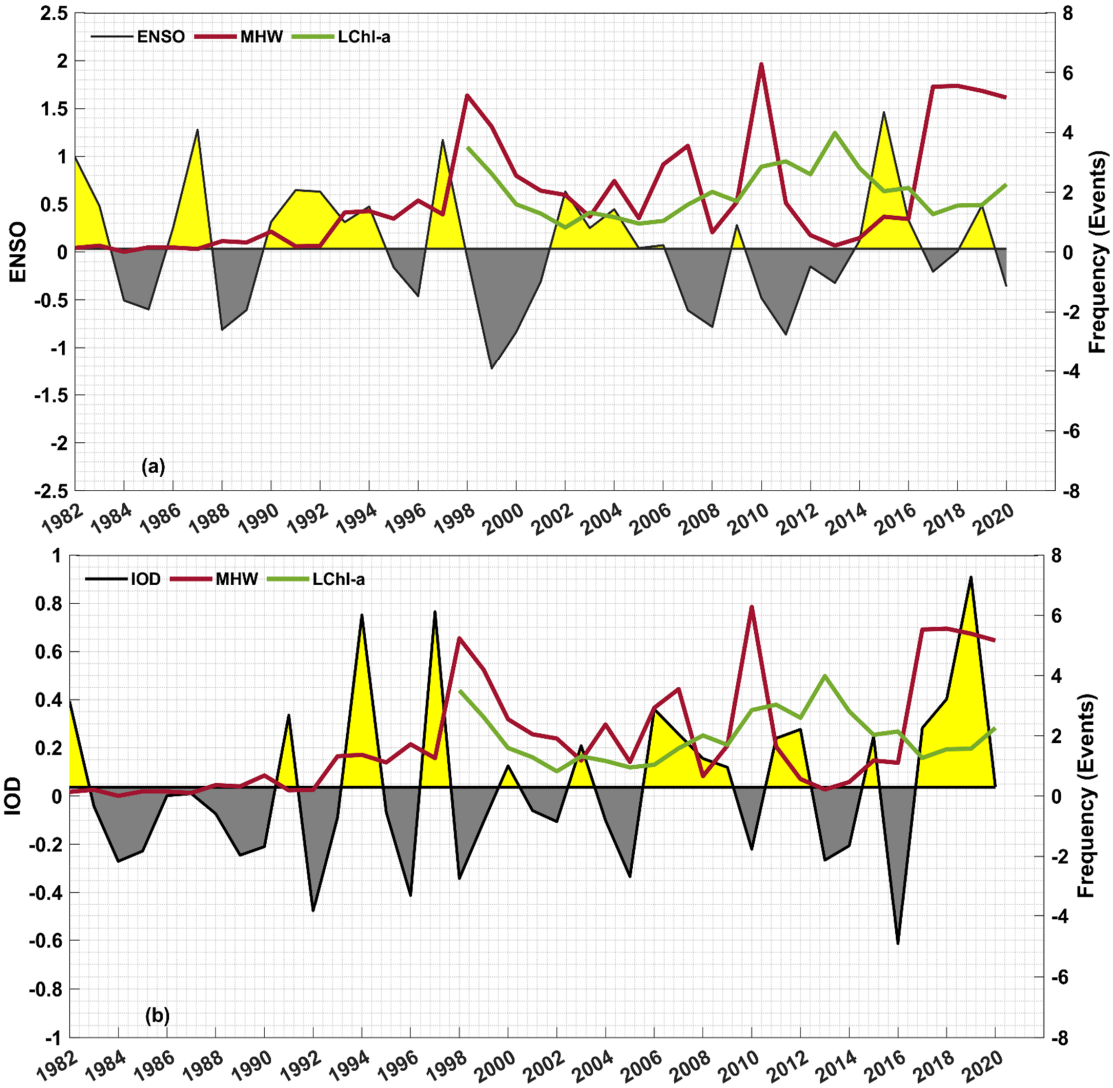


**Figure 9.** The annual time series of the normalized Niño 3.4 (ENSO) (shading, in (**a**)) and the Indian Ocean Dipole (IOD) (shading, in (**b**)), with the annual MHW frequency of (solid red line) from 1982 to 2020, and annual LChl-a frequency (solid green line) from 1998 to 2020 for the entire study area. The yellow and grey shading refer to the positive and negative phases of the climate indices, respectively.

### *3.6. The Compound MHW and LChl-a Event in 2020 and Its Relation to Atmospheric Forcings*

The longest compound MHW and LChl-a event during the study period (1998–2020) was observed at OG in 2020 (Figure 10). This prolonged MHW event lasted for two months (29 June–29 August 2020), while the co-occurrence of MHW and LChl-a events lasted for 42 days (10 July–21 August 2020) (Figure 10a). According to the MHW classification of Hobday et.al., 2018 [19], the intensity of this MHW ranged from moderate (i.e., SST exceeded the 90th percentile threshold) to severe (i.e., SST exceeded three times the 90th percentile threshold). During this event, the mean and maximum MHW intensities are 3.5 and 5.3 °C, respectively. The LChl-a event occurred with a delay of 11 days after the beginning of the MHW event and ended when the MHW began to decay (7 days before the end of the MHW event). The mean and maximum intensities of the LChl-a event were −0.82 and −0.90 mg/m$^3$, respectively.

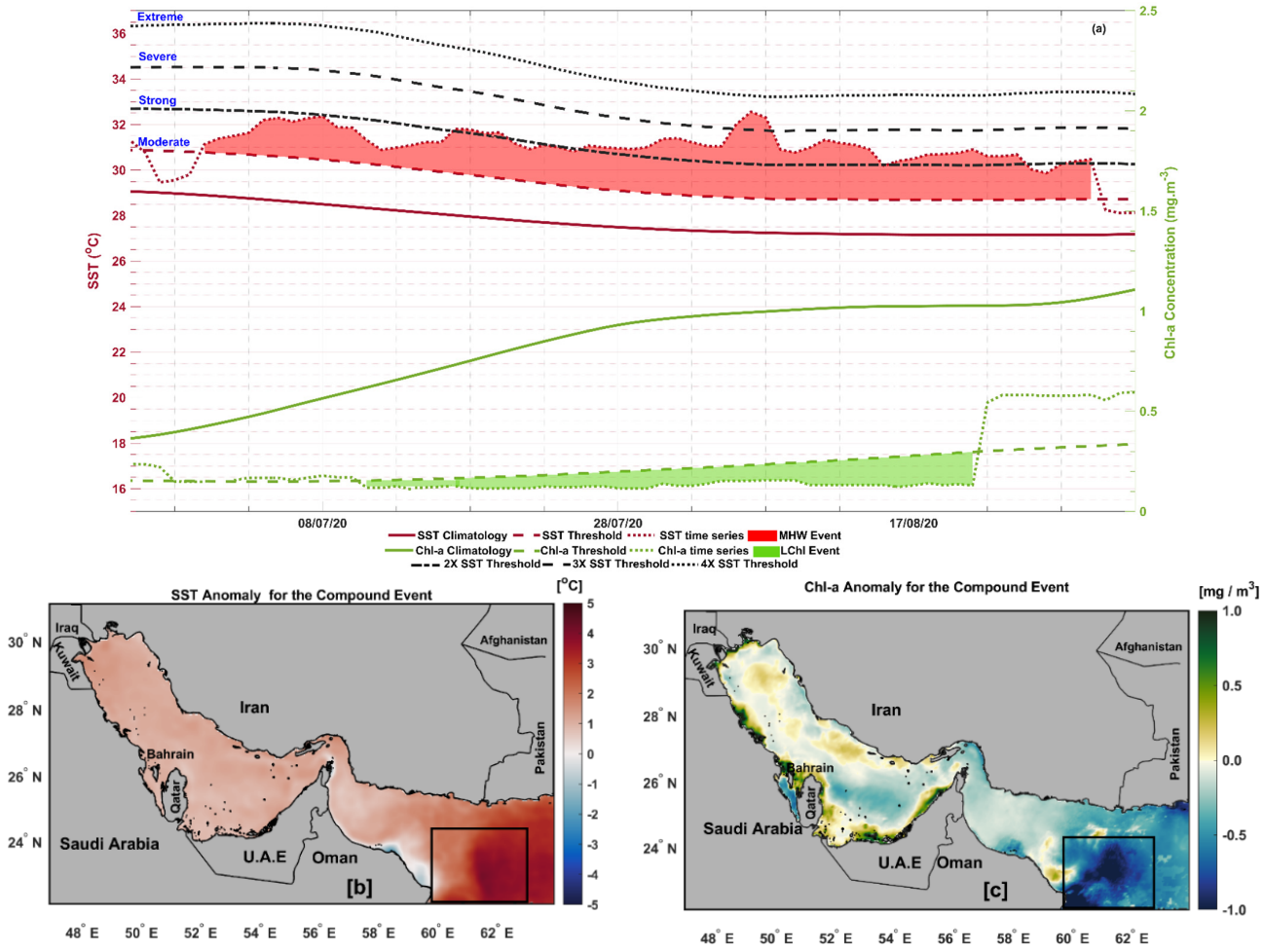


**Figure 10.** (**a**) The longest compound MHW and LChl-a event. The red shaded area refers to the MHW event, while the green one represents the LChl-a event. The black dotted line defines the MHW categories (moderate, strong, severe, and extreme), (**b**) the SSTA (°C), and (**c**) the Chl-a anomaly (mg/m$^3$) averaged during the compound event (10 July to 21 August 2020). Note that the anomalies are calculated with respect to the period [1998–2020]. The black rectangle in b and c defines the area that was affected by the compound event.

Figure 10b shows the spatial distribution of SSTA over the entire region during the compound event. Positive SSTA was observed throughout the region (AG and OG), except for the southeastern coast of Oman, where negative SSTA was observed. The highest SSTA was detected in the southern part of OG (bounded by the black box in Figure 10b), with values up to 5 °C above average. The spatial distribution of the Chl-a anomaly during

the compound event is shown in Figure 10c. The lowest Chl-a concentration anomaly (~−1 mg/m$^3$) was found in the same region with the highest SSTA. The highest positive Chl-a anomaly was observed along the coastal areas, especially within AG (i.e., along the coasts of Saudi Arabia, Bahrain, Qatar, and the United Arab Emirates). According to [44,47–49], these coastal areas in AG generally exhibit the highest sea surface productivity.

In this part, we try to investigate the possible link between MHW and LChl-a compound event with 2-m air temperature, surface net heat flux, and wind stress, (Figures 11 and 12). The atmospheric states during the compound event (21 July to 29 August 2020) revealed a warm atmospheric temperature over the whole study region with the highest value over the AG. Positive 2-m air temperature anomalies were found across most of the region, with the highest values (>+2 °C) observed in the OG (black rectangle in Figure 11b), which coincides with the same region of the compound event. The spatial distribution of the total surface net heat flux and its anomaly during the compound event is shown in Figure 11c,d. The highest total surface net heat flux (>+80 W/m$^2$) is observed in the central part of the study region, while the lowest (<+20 W/m$^2$) is found in the northern and southeastern parts of the study area. The negative anomaly pattern of the total heat flux (i.e., loss; <−60 W/m$^2$) is found in the same region of the compound event (see black box; Figure 11d), indicating upward heat loss, which could be an indicator of higher SSTA during this compound event.

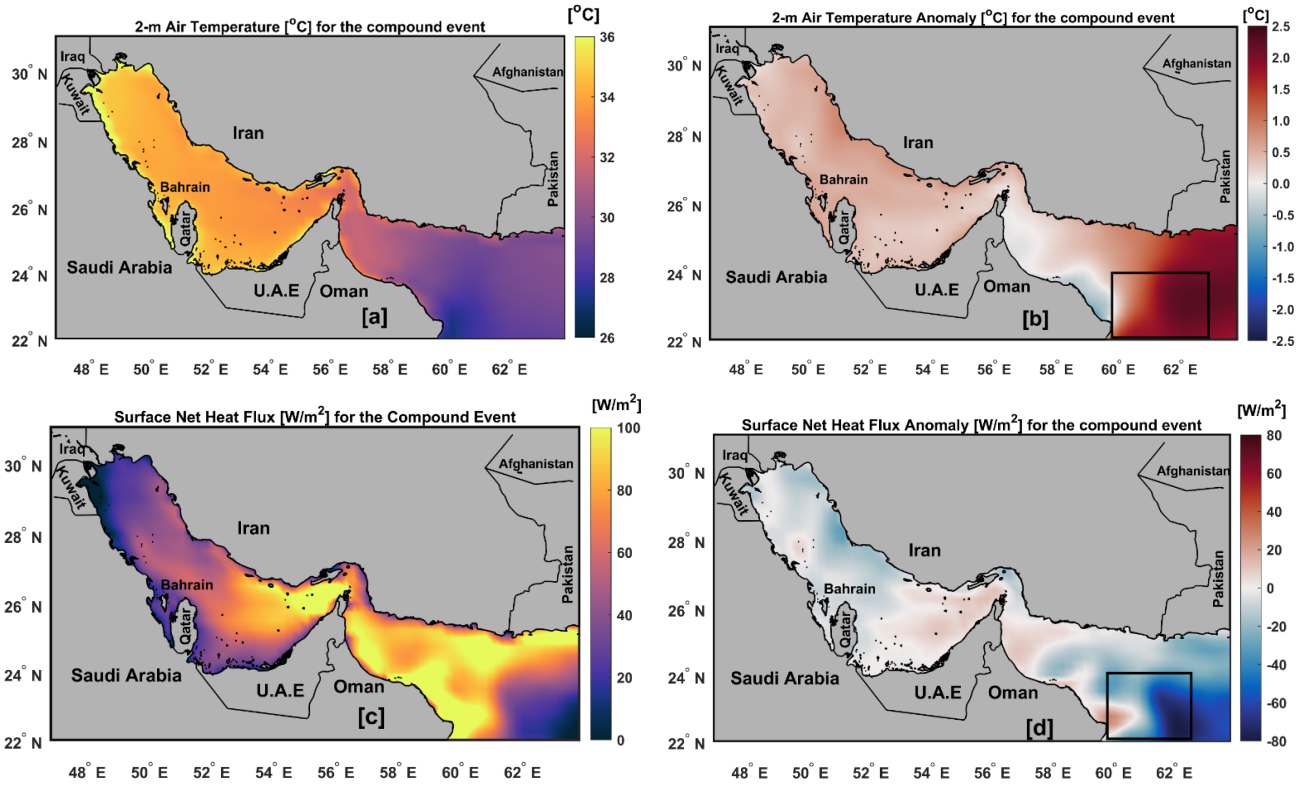


**Figure 11.** The mean (**a**) and anomaly (**b**) of the 2-m air temperature in [°C]. The mean (**c**) and anomaly (**d**) of the total net surface heat flux in [W/m$^2$] during the longest compound MHW and LChl-a event (10 July–21 August 2020). Note that the anomalies were calculated with respect to the period [1982–2020] from the hourly ERA5 data. The black rectangle in (**b**,**d**) defines the area that was affected by the compound event.

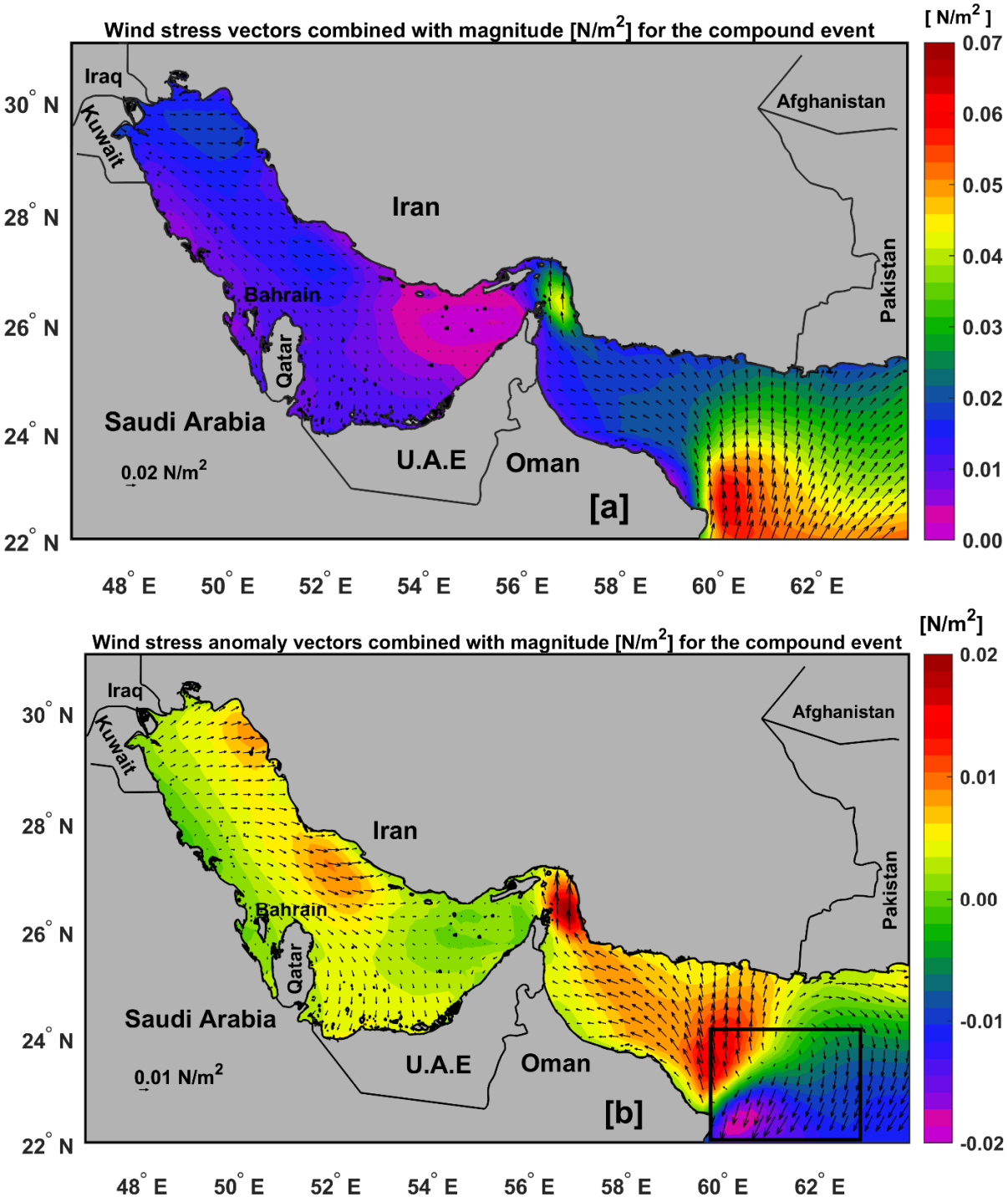


**Figure 12.** The mean (**a**) and anomaly (**b**) of wind stress vectors (black arrows) combined with magnitude (shading) in [N/m$^2$] during the longest compound MHW and LChl-a event (10 July to 21 August 2020). Note that the anomalies are calculated with respect to the period [1982–2020] from the hourly ERA5 data. The black rectangle in (**b**) defines the area that was affected by the compound event.

The dominant wind stress pattern during this event was summer southwesterly monsoon winds over the OG region, while weak northwesterly winds (Shamal) prevailed in AG (Figure 12a), which is consistent with [87,88]. The lowest negative wind stress anomaly (i.e., from −0.02 to 0 N/m$^2$) is observed in the area affected by the compound event in OG (Figure 12b), which has the highest SST and the lowest Chl-a anomalies (Figure 10b,c). This

reduction in wind stress is most likely associated with the formation of the MHW and the compound event. These results are consistent with previous studies [4,26,89,90] that found that MHW extreme events are associated with wind reduction.

## 4. Discussion

In this work, we investigated the spatio-temporal variability and trend of SSTs and MHWs in AG and OG during the period 1982 to 2020 using high-resolution remote sensing data. In addition, to the best of our knowledge, we examined for the first time the compound events (MHWs and LChl-a) and their relationship with atmospheric parameters and climate indices (i.e., ENSO and IOD) in AG and OG.

The results revealed that the average SST climatology across the study region ranged from 23 to 28 °C (Figure 2a). The lowest values (<24 °C) of SST climatology were found in the northern part of AG off the Kuwaiti and Iraqi coasts, while the highest values (>28 °C) were found in the northern part of OG off the Omani coast (Figure 2a). A highly significant ($p < 0.05$) spatial SST trend was observed in the study area (Figure 2b), with a warming trend ranging from +0.15 to +0.65 °C/decade during the study period from 1982 to 2020. The temporal SST trends between 1982 to 2020 were about 0.44 ± 0.06 °C/decade and 0.32 ± 0.04 °C/decade for AG and OG, respectively (Figure 3a,b). This result is in good agreement with [33], who found that the average SST trend was about 0.41 ± 0.14 °C/decade in the AG during the same period (1982–2020).

The highest number of MHW events (~7 events/year) was observed in 2010 at AG (Figure 4a). This peak coincides with a high SSTA (~2 °C) that year (Figure 3a) and the strongest negative phase of ENSO (i.e., La Niña) that occurred in the same year (Figure 9a). The high SST values observed in 2010 were subjected to ENSO [85,86]. A strong relationship was found between SST and the annual MHW frequency, with correlation coefficients of 0.84 and 0.88 for AG and OG, respectively (Figure 4c). Overall, the spatial distribution of mean MHW characteristics (Figure 5a,b) showed that AG was characterized by long-lasting and less frequent MHWs, whereas OG was characterized by high frequency and short duration. The highest annual MHW frequency trend (up to 1.5 events/decade) was detected in the northern part of OG (Figure 5c). The maximum and most significant annual MHW duration trend (>6 days/decade) was found in the northwestern part of AG (i.e., the same regions that showed the highest SST trend; see Figure 2b) and the southeastern part of OG (Figure 5d). The annual MHW frequency trend was about 0.97 events/decade for the entire study region from 1982 to 2020. While a non-significant trend was found for the annual MHW duration with an average of 2.3 days/decade for the study area. These results are in line with those of [28], who discovered an increasing trend in the frequency of MHW in the northern Arabian Sea region at a rate of about 1 event/decade.

The spatial distribution of mean intensity and duration of MHW and LChl-a events as well as their correlation maps from 1998 to 2020 were shown in Figures 7 and 8. The largest negative anomalies in Chl-a concentration (<−0.75 mg/m$^3$) were found in the coastal areas of OG, the northern tip of AG near the Shatt-Al-Arab River, and off the southeast coast of Bahrain. At the same time, these areas also have high mean MHW intensity (>1.5 °C; Figure 7b) and the highest correlation (> 0.6; Figure 7c). The longest duration of MHW (>14 days) and LChl-a (>13 days) was found in the southern part of OG, and this particular region had the highest correlation (>0.7) between them (Figure 8a–c). La Niña events in 1999, 2010, 2011, and 2020 were associated with higher frequencies of MHW and LChl-a (Figure 9a). While the positive phase of IOD coincided with high MHW frequency in 2018 and 2019 (Figure 9b).

We noted the longest compound event in the southern part of OG, which lasted 42 days (10 July–21 August 2020; Figure 10a). The LChl-a event occurred with a delay of 11 days after the onset of the MHW event and ended when the MHW began to decay (7 days before the end of the MHW event). The maximum intensity of the LChl-a and MHW events was −0.90 mg/m$^3$ and 5.3 °C, respectively (Figure 10b,c). The dominant wind stress pattern during this event was summer southwesterly monsoon winds over the OG region

(Figure 12a), which is consistent with [87,88]. In conclusion, during this compound event, the SST and Chl-a anomalies were associated with a high air temperature anomaly and a reduction in wind stress anomaly (Figures 11 and 12). These results are in line with previous studies [4,26,89,90], which found that MHW extreme events are generally associated with high air temperature and a decrease in winds.

## 5. Conclusions

In summary, our study revealed an SST warming trend of about 0.4 °C/decade for the entire study region. This SST warming trend resulted in a positive trend in the frequency and duration of MHW, which in turn contributed to the decline in surface productivity in the study area. MHW can severely impact the marine environment, and LChl-a also threatens marine ecosystems that rely on phytoplankton as the basis of their food web [38], so the compound between the two extreme events in our study region could have devastating effects on marine life. For future work, further research is needed to examine the combination between the MHW and other biogeochemical components (e.g., extreme nutrient- and oxygen-depleted events) beyond the LChl-a to provide a comprehensive assessment of their consequences on the marine environment.

**Author Contributions:** Conceptualization M.H., B.M., O.I. and H.N.; methodology M.H., H.N., O.I. and B.M.; formal analysis M.H., B.M., H.N. and O.I.; investigation M.H., B.M., O.I. and H.N.; resources M.H., O.I., B.M. and H.N.; data curation M.H., O.I., H.N. and B.M.; writing—original draft preparation M.H., B.M., O.I. and H.N.; writing—review and editing M.H., H.N., B.M. and O.I.; visualization M.H., O.I., B.M. and H.N.; supervision M.H., H.N., O.I. and B.M. All authors have read and agreed to the published version of the manuscript.

**Funding:** This research received no external funding.

**Data Availability Statement:** The datasets used in this work are publicly available online through the Copernicus Marine Environment Monitoring Service (CMEMS) (CMEMS; https://resources.marine.copernicus.eu/?option=com_csw&view=details&product_id=SST_GLO_SST_L4_REP_OBSERVATIONS_010_011; downloaded on 22 February 2022); Daily Chl-a concentration data are obtained from CMEMS (Data | Copernicus Marine; downloaded on 15 March 2022); the atmospheric data are obtained from the European Centre for Medium-Range Weather Forecasts (ECMWF) ERA5 (https://cds.climate.copernicus.eu/cdsapp#!/dataset/reanalysis-era5-single-levels (downloaded on 20 April 2022); El Niño-Southern Oscillation (ENSO) was obtained from (https://psl.noaa.gov/data/climateindices/list/; accessed 28 August 2022). The Indian Ocean Dipole (IOD) was downloaded from Japan Agency for Marine-Earth Science and Technology (JAMSTEC) (https://www.jamstec.go.jp/virtualearth/general/en/; accessed 28 August 2022).

**Acknowledgments:** The authors would like to express their appreciation to the anonymous reviewers for their constructive comments. The authors would like to express their gratitude to the Copernicus Marine Environment Monitoring Service (CMEMS) project for supplying the SST dataset used in this investigation. The authors would like to express their gratitude to Kieran Lyons from the Marine Institute in Ireland for his assistance in the linguistic editing of our manuscript.

**Conflicts of Interest:** The authors declare no conflict of interest.

## References

1. Oliver, E.C.J.; Donat, M.G.; Burrows, M.T.; Moore, P.J.; Smale, D.A.; Alexander, L.V.; Benthuysen, J.A.; Feng, M.; Gupta, A.S.; Hobday, A.J.; et al. Longer and more frequent marine heatwaves over the past century. *Nat. Commun.* **2018**, *9*, 1324. [CrossRef] [PubMed]
2. Jacox, M.G.; Alexander, M.A.; Amaya, D.; Becker, E.; Bograd, S.J.; Brodie, S.; Hazen, E.L.; Buil, M.P.; Tommasi, D. Global seasonal forecasts of marine heatwaves. *Nature* **2022**, *604*, 486–490. [CrossRef] [PubMed]
3. Kuroda, H.; Setou, T. Extensive Marine Heatwaves at the Sea Surface in the Northwestern Pacific Ocean in Summer 2021. *Remote Sens.* **2021**, *13*, 3989. [CrossRef]
4. Ibrahim, O.; Mohamed, B.; Nagy, H. Spatial Variability and Trends of Marine Heat Waves in the Eastern Mediterranean Sea over 39 Years. *J. Mar. Sci. Eng.* **2021**, *9*, 643. [CrossRef]
5. Mohamed, B.; Nagy, H.; Ibrahim, O. Spatiotemporal Variability and Trends of Marine Heat Waves in the Red Sea over 38 Years. *J. Mar. Sci. Eng.* **2021**, *9*, 842. [CrossRef]

6. Mohamed, B.; Ibrahim, O.; Nagy, H. Sea Surface Temperature Variability and Marine Heatwaves in the Black Sea. *Remote Sens.* **2022**, *14*, 2383. [CrossRef]
7. Hughes, T.P.; Anderson, K.D.; Connolly, S.R.; Heron, S.F.; Kerry, J.T.; Lough, J.M.; Baird, A.H.; Baum, J.K.; Berumen, M.L.; Bridge, T.C.; et al. Spatial and temporal patterns of mass bleaching of corals in the Anthropocene. *Science* **2018**, *359*, 80–83. [CrossRef]
8. Garrabou, J.; Coma, R.; Bensoussan, N.; Bally, M.; Chevaldonné, P.; Cigliano, M.; Diaz, D.; Harmelin, J.G.; Gambi, M.C.; Kersting, D.K.; et al. Mass mortality in Northwestern Mediterranean rocky benthic communities: Effects of the 2003 heat wave. *Glob. Chang. Biol.* **2009**, *15*, 1090–1103. [CrossRef]
9. Trainer, V.L.; Kudela, R.M.; Hunter, M.V.; Adams, N.G.; McCabe, R.M. Climate Extreme Seeds a New Domoic Acid Hotspot on the US West Coast. *Front. Clim.* **2020**, *2*, 571836. [CrossRef]
10. Bond, N.A.; Cronin, M.F.; Freeland, H.; Mantua, N. Causes and impacts of the 2014 warm anomaly in the NE Pacific. *Geophys. Res. Lett.* **2015**, *42*, 3414–3420. [CrossRef]
11. Le Grix, N.; Zscheischler, J.; Laufkötter, C.; Rousseaux, C.S.; Frölicher, T.L. Compound high-temperature and low-chlorophyll extremes in the ocean over the satellite period. *Biogeosciences* **2021**, *18*, 2119–2137. [CrossRef]
12. Smale, D.A.; Wernberg, T.; Oliver, E.C.J.; Thomsen, M.; Harvey, B.P.; Straub, S.C.; Burrows, M.T.; Alexander, L.V.; Benthuysen, J.A.; Donat, M.G.; et al. Marine heatwaves threaten global biodiversity and the provision of ecosystem services. *Nat. Clim. Chang.* **2019**, *9*, 306–312. [CrossRef]
13. Benthuysen, J.A.; Oliver, E.C.J.; Chen, K.; Wernberg, T. Editorial: Advances in Understanding Marine Heatwaves and Their Impacts. *Front. Mar. Sci.* **2020**, *7*, 147. [CrossRef]
14. Arafeh-Dalmau, N.; Montaño-Moctezuma, G.; Martínez, J.A.; Beas, R.; Schoeman, D.; Torres-Moye, G. Extreme Marine Heatwaves Alter Kelp Forest Community Near Its Equatorward Distribution Limit. *Front. Mar. Sci.* **2019**, *6*, 499. [CrossRef]
15. Mills, K.E.; Pershing, A.J.; Brown, C.J.; Chen, Y.; Chiang, F.-S.; Holland, D.S.; Lehuta, S.; Nye, J.A.; Sun, J.C.; Thomas, A.C.; et al. Fisheries Management in a Changing Climate: Lessons From the 2012 Ocean Heat Wave in the Northwest Atlantic. *Oceanography* **2013**, *26*, 191–195. [CrossRef]
16. Hobday, A.J.; Alexander, L.V.; Perkins, S.E.; Smale, D.A.; Straub, S.C.; Oliver, E.C.J.; Benthuysen, J.A.; Burrows, M.T.; Donat, M.G.; Feng, M.; et al. A hierarchical approach to defining marine heatwaves. *Prog. Oceanogr.* **2016**, *141*, 227–238. [CrossRef]
17. Di Lorenzo, E.; Mantua, N. Multi-Year Persistence of the 2014/15 North Pacific Marine Heatwave. *Nat. Clim. Chang.* **2016**, *6*, 1042. [CrossRef]
18. Miyama, T.; Minobe, S.; Goto, H. Marine Heatwave of Sea Surface Temperature of the Oyashio Region in Summer in 2010–2016. *Front. Mar. Sci.* **2021**, *7*, 576240. [CrossRef]
19. Hobday, A.J.; Oliver, E.C.J.; Gupta, A.S.; Benthuysen, J.A.; Burrows, M.T.; Donat, M.G.; Holbrook, N.J.; Moore, P.J.; Thomsen, M.S.; Wernberg, T.; et al. Categorizing and Naming Marine Heatwaves. *Oceanography* **2018**, *31*, 162–173. [CrossRef]
20. Rivetti, I.; Fraschetti, S.; Lionello, P.; Zambianchi, E.; Boero, F. Global Warming and Mass Mortalities of Benthic Invertebrates in the Mediterranean Sea. *PLoS ONE* **2014**, *9*, e115655. [CrossRef]
21. Mavrakis, A.F.; Tsiros, I.X. The abrupt increase in the Aegean sea surface temperature during June 2007—A marine heatwave event? *Weather* **2018**, *74*, 201–207. [CrossRef]
22. Darmaraki, S.; Somot, S.; Sevault, F.; Nabat, P. Past Variability of Mediterranean Sea Marine Heatwaves. *Geophys. Res. Lett.* **2019**, *46*, 9813–9823. [CrossRef]
23. Darmaraki, S.; Somot, S.; Sevault, F.; Nabat, P.; Narvaez, W.D.C.; Cavicchia, L.; Djurdjevic, V.; Li, L.; Sannino, G.; Sein, D.V. Future evolution of Marine Heatwaves in the Mediterranean Sea. *Clim. Dyn.* **2019**, *53*, 1371–1392. [CrossRef]
24. Oliver, E.C.; Benthuysen, J.A.; Bindoff, N.L.; Hobday, A.J.; Holbrook, N.J.; Mundy, C.N.; Perkins-Kirkpatrick, S.E. The Unprecedented 2015/16 Tasman Sea Marine Heatwave. *Nat. Commun.* **2017**, *8*, 16101. [CrossRef] [PubMed]
25. Alawad, K.; Al-Subhi, A.; Alsaafani, M.; Alraddadi, T. Atmospheric Forcing of the High and Low Extremes in the Sea Surface Temperature over the Red Sea and Associated Chlorophyll-a Concentration. *Remote Sens.* **2020**, *12*, 2227. [CrossRef]
26. Mohamed, B.; Nilsen, F.; Skogseth, R. Marine Heatwaves Characteristics in the Barents Sea Based on High Resolution Satellite Data (1982–2020). *Front. Mar. Sci.* **2022**, *9*, 821646. [CrossRef]
27. Saranya, J.S.; Roxy, M.K.; Dasgupta, P.; Anand, A. Genesis and Trends in Marine Heatwaves Over the Tropical Indian Ocean and Their Interaction with the Indian Summer Monsoon. *J. Geophys. Res. Oceans* **2022**, *127*, e2021JC017427. [CrossRef]
28. Chatterjee, A.; Anil, G.; Shenoy, L.R. Marine heatwaves in the Arabian Sea. *Ocean Sci.* **2022**, *18*, 639–657. [CrossRef]
29. Riegl, B.; Purkis, S. Persian/Arabian Gulf Coral Reefs. In *Encyclopedia of Modern Coral Reefs*; Hopley, D., Ed.; Springer: Dordrecht, The Netherlands, 2011; pp. 790–798.
30. Johns, W.E.; Yao, F.; Olson, D.B.; Josey, S.A.; Grist, J.P.; Smeed, D.A. Observations of seasonal exchange through the Straits of Hormuz and the inferred heat and freshwater budgets of the Persian Gulf. *J. Geophys. Res. Earth Surf.* **2003**, *108*, C12. [CrossRef]
31. Khan, S.; Piao, S.; Khan, I.U.; Xu, B.; Khan, S.; Ismail, M.A.; Song, Y. Variability of SST and ILD in the Arabian Sea and Sea of Oman in Association with the Monsoon Cycle. *Math. Probl. Eng.* **2021**, *2021*, 9958257. [CrossRef]
32. Riegl, B.M.; Purkis, S.J.; Al-Cibahy, A.S.; Abdel-Moati, M.A.; Hoegh-Guldberg, O. Present Limits to Heat-Adaptability in Corals and Population-Level Responses to Climate Extremes. *PLoS ONE* **2011**, *6*, e24802. [CrossRef] [PubMed]
33. Al Senafi, F. Atmosphere-Ocean Coupled Variability in the Arabian/Persian Gulf. *Front. Mar. Sci.* **2022**, *9*, 809355. [CrossRef]

34. Al-Yamani, F.Y.; Polikarpov, I.; Saburova, M. Marine life mortalities and Harmful Algal Blooms in the Northern Arabian Gulf. *Aquat. Ecosyst. Health Manag.* **2020**, *23*, 196–209. [CrossRef]
35. Watanabe, T.K.; Watanabe, T.; Yamazaki, A.; Pfeiffer, M.; Garbe-Schönberg, D.; Claereboudt, M.R. Past summer upwelling events in the Gulf of Oman derived from a coral geochemical record. *Sci. Rep.* **2017**, *7*, 4568. [CrossRef] [PubMed]
36. Al-Azri, A.R.; Piontkovski, S.A.; Al-Hashmi, K.A.; Goes, J.I.; Gomes, H.R.D. Chlorophyll a as a measure of seasonal coupling between phytoplankton and the monsoon periods in the Gulf of Oman. *Aquat. Ecol.* **2009**, *44*, 449–461. [CrossRef]
37. Wiggert, J.; Hood, R.; Banse, K.; Kindle, J. Monsoon-driven biogeochemical processes in the Arabian Sea. *Prog. Oceanogr.* **2005**, *65*, 176–213. [CrossRef]
38. Cavole, L.M.; Demko, A.M.; Diner, R.E.; Giddings, A.; Koester, I.; Pagniello, C.M.; Franks, P.J. Biological Impacts of the 2013–2015 Warm-Water Anomaly in the Northeast Pacific: Winners, Losers, and the Future. *Oceanography* **2016**, *29*, 273–285. [CrossRef]
39. Leonard, M.; Westra, S.; Phatak, A.; Lambert, M.; van den Hurk, B.; McInnes, K.; Risbey, J.; Schuster, S.; Jakob, D.; Stafford-Smith, M. A compound event framework for understanding extreme impacts. *WIREs Clim. Chang.* **2014**, *5*, 113–128. [CrossRef]
40. Ipcc. *The Ocean and Cryosphere in a Changing Climate: Special Report of the Intergovernmental Panel on Climate Change*, 1st ed.; Cambridge University Press: Cambridge, UK, 2022.
41. Montie, S.; Thomsen, M.S.; Rack, W.; Broady, P.A. Extreme summer marine heatwaves increase chlorophyll *a* in the Southern Ocean. *Antarct. Sci.* **2020**, *32*, 508–509. [CrossRef]
42. Noh, K.M.; Lim, H.-G.; Kug, J.-S. Global chlorophyll responses to marine heatwaves in satellite ocean color. *Environ. Res. Lett.* **2022**, *17*, 064034. [CrossRef]
43. Ghasemifar, E.; Farajzadeh, M.; Mohammadi, C.; Alipoor, E. Long-Term Change of Surface Temperature in Water Bodies around Iran—Caspian Sea, Gulf of Oman, and Persian Gulf—Using 2001–2015 MODIS Data. *Phys. Geogr.* **2020**, *41*, 21. [CrossRef]
44. Moradi, M. Trend analysis and variations of sea surface temperature and chlorophyll-a in the Persian Gulf. *Mar. Pollut. Bull.* **2020**, *156*, 111267. [CrossRef] [PubMed]
45. Alosairi, Y.; Alsulaiman, N.; Rashed, A.; Al-Houti, D. World record extreme sea surface temperatures in the northwestern Arabian/Persian Gulf verified by in situ measurements. *Mar. Pollut. Bull.* **2020**, *161*, 111766. [CrossRef] [PubMed]
46. Nesterov, O.; Temimi, M.; Fonseca, R.; Nelli, N.R.; Addad, Y.; Bosc, E.; Abida, R. Validation and statistical analysis of the Group for High Resolution Sea Surface Temperature data in the Arabian Gulf. *Oceanologia* **2021**, *63*, 497–515. [CrossRef]
47. Nezlin, N.; Polikarpov, I.; Al-Yamani, F. Satellite-Measured Chlorophyll Distribution in the Arabian Gulf: Spatial, Seasonal and Inter-Annual Variability. *Int. J. Oceans Oceanogr.* **2007**, *2*, 139.
48. Nezlin, N.P.; Polikarpov, I.; Al-Yamani, F.Y.; Rao, D.S.; Ignatov, A. Satellite monitoring of climatic factors regulating phytoplankton variability in the Arabian (Persian) Gulf. *J. Mar. Syst.* **2010**, *82*, 47–60. [CrossRef]
49. Moradi, M.; Kabiri, K. Spatio-temporal variability of SST and Chlorophyll-a from MODIS data in the Persian Gulf. *Mar. Pollut. Bull.* **2015**, *98*, 14–25. [CrossRef]
50. Hussein, K.; Al Abdouli, K.; Ghebreyesus, D.; Petchprayoon, P.; Al Hosani, N.; Sharif, H.O. Spatiotemporal Variability of Chlorophyll-a and Sea Surface Temperature, and Their Relationship with Bathymetry over the Coasts of UAE. *Remote Sens.* **2021**, *13*, 2447. [CrossRef]
51. Al-Shehhi, M.R.; Nelson, D.; Farzanah, R.; Alshihi, R.; Salehi-Ashtiani, K. Characterizing algal blooms in a shallow & a deep channel. *Ocean Coast. Manag.* **2021**, *213*, 105840. [CrossRef]
52. Al Senafi, F.; Anis, A. Internal Waves on the Continental Shelf of the Northwestern Arabian Gulf. *Front. Mar. Sci.* **2020**, *6*, 00805. [CrossRef]
53. Rio, M.H.; Guinehut, S.; Larnicol, G. New CNES-CLS09 Global Mean Dynamic Topography Computed from the Combination of GRACE Data, Altimetry, and in Situ Measurements. *J. Geophys. Res. Oceans* **2011**, *116*, C7. [CrossRef]
54. Mulet, S.; Rio, M.-H.; Etienne, H.; Artana, C.; Cancet, M.; Dibarboure, G.; Feng, H.; Husson, R.; Picot, N.; Provost, C.; et al. The new CNES-CLS18 global mean dynamic topography. *Ocean Sci.* **2021**, *17*, 789–808. [CrossRef]
55. Schott, F.; Swallow, J.C.; Fieux, M. The Somali current at the equator: Annual cycle of currents and transports in the upper 1000 m and connection to neighbouring latitudes. *Deep Sea Res. Part A Oceanogr. Res. Pap.* **1990**, *37*, 1825–1848. [CrossRef]
56. Brock, J.C.; McClain, C.R. Interannual variability in phytoplankton blooms observed in the northwestern Arabian Sea during the southwest monsoon. *J. Geophys. Res. Earth Surf.* **1992**, *97*, 733. [CrossRef]
57. Burkill, P.; Mantoura, R.; Owens, N. Biogeochemical cycling in the northwestern Indian Ocean: A brief overview. *Deep Sea Res. Part II Top. Stud. Oceanogr.* **1993**, *40*, 643–649. [CrossRef]
58. Savidge, G.; Lennon, J.; Matthews, A.J. A shore-based survey of upwelling along the coast of Dhofar region, southern Oman. *Cont. Shelf Res.* **1990**, *10*, 259–275. [CrossRef]
59. Kämpf, J.; Sadrinasab, M. The circulation of the Persian Gulf: A numerical study. *Ocean Sci.* **2006**, *2*, 27–41. [CrossRef]
60. Al-Shehhi, M.R.; Song, H.; Scott, J.; Marshall, J. Water mass transformation and overturning circulation in the Arabian Gulf. *J. Phys. Oceanogr.* **2021**, *51*, 3513–3527. [CrossRef]
61. Al Senafi, F.; Anis, A. Shamals and climate variability in the Northern Arabian/Persian Gulf from 1973 to 2012. *Int. J. Clim.* **2015**, *35*, 4509–4528. [CrossRef]
62. Chao, S.-Y.; Kao, T.W.; Al-Hajri, K.R. A Numerical Investigation of Circulation in the Arabian Gulf. *J. Geophys. Res. Earth Surf.* **1992**, *97*, 11219–11236. [CrossRef]

63. Giannakopoulou, E.M.; Toumi, R. The Persian Gulf Summertime Low-Level Jet over Sloping Terrain: The Persian Gulf Summertime Low-Level Jet. *Q. J. R. Meteorol. Soc.* **2012**, *138*, 145. [CrossRef]
64. Good, S.; Fiedler, E.; Mao, C.; Martin, M.J.; Maycock, A.; Reid, R.; Roberts-Jones, J.; Searle, T.; Waters, J.; While, J.; et al. The Current Configuration of the Ostia System for Operational Production of Foundation Sea Surface Temperature and Ice Concentration Analyses. *Remote Sens.* **2020**, *12*, 720. [CrossRef]
65. Fiedler, S.; Crueger, T.; D'Agostino, R.; Peters, K.; Becker, T.; Leutwyler, D.; Paccini, L.; Burdanowitz, J.; Buehler, S.A.; Cortes, A.U.; et al. Simulated Tropical Precipitation Assessed across Three Major Phases of the Coupled Model Intercomparison Project (CMIP). *Mon. Weather Rev.* **2020**, *148*, 3653–3680. [CrossRef]
66. Hersbach, H.; Bell, B.; Berrisford, P.; Hirahara, S.; Horanyi, A.; Muñoz-Sabater, J.; Nicolas, J.; Peubey, C.; Radu, R.; Schepers, D.; et al. The ERA5 global reanalysis. *Q. J. R. Meteorol. Soc.* **2020**, *146*, 1999–2049. [CrossRef]
67. Huang, B.; Thorne, P.W.; Banzon, V.F.; Boyer, T.; Chepurin, G.; Lawrimore, J.H.; Menne, M.J.; Smith, T.M.; Vose, R.S.; Zhang, H.-M. Extended Reconstructed Sea Surface Temperature, Version 5 (ERSSTv5): Upgrades, Validations, and Intercomparisons. *J. Clim.* **2017**, *30*, 8179–8205. [CrossRef]
68. Saji, N.H.; Goswami, B.N.; Vinayachandran, P.N.; Yamagata, T. A dipole mode in the tropical Indian Ocean. *Nature* **1999**, *401*, 360–363. [CrossRef]
69. Zhao, Z.; Marin, M. A MATLAB toolbox to detect and analyze marine heatwaves. *J. Open Source Softw.* **2019**, *4*, 1124. [CrossRef]
70. Sen, P.K. Estimates of the Regression Coefficient Based on Kendall's Tau. *J. Am. Stat. Assoc.* **1968**, *63*, 1379. [CrossRef]
71. Hamed, K.H.; Rao, A.R. A modified Mann-Kendall trend test for autocorrelated data. *J. Hydrol.* **1998**, *204*, 182–196. [CrossRef]
72. Wang, F.; Shao, W.; Yu, H.; Kan, G.; He, X.; Zhang, D.; Ren, M.; Wang, G. Re-evaluation of the Power of the Mann-Kendall Test for Detecting Monotonic Trends in Hydrometeorological Time Series. *Front. Earth Sci.* **2020**, *8*, 00014. [CrossRef]
73. Pinardi, N.; Allen, I.; Demirov, E.; De Mey, P.; Korres, G.; Lascaratos, A.; Le Traon, P.-Y.; Maillard, C.; Manzella, G.; Tziavos, C. The Mediterranean ocean forecasting system: First phase of implementation (1998–2001). *Ann. Geophys.* **2003**, *21*, 3–20. [CrossRef]
74. Nagy, H.; Elgindy, A.; Pinardi, N.; Zavatarelli, M.; Oddo, P. A nested pre-operational model for the Egyptian shelf zone: Model configuration and validation/calibration. *Dyn. Atmos. Oceans* **2017**, *80*, 75–96. [CrossRef]
75. Nagy, H.; Mohamed, B.; Ibrahim, O. Variability of Heat and Water Fluxes in the Red Sea Using ERA5 Data (1981–2020). *J. Mar. Sci. Eng.* **2021**, *9*, 1276. [CrossRef]
76. Zhang, Y.; Rossow, W.B.; Lacis, A.A.; Oinas, V.; Mishchenko, M. Calculation of radiative fluxes from the surface to top of atmosphere based on ISCCP and other global data sets: Refinements of the radiative transfer model and the input data. *J. Geophys. Res. Earth Surf.* **2004**, *109*, D19. [CrossRef]
77. Kumar, B.P.; Vialard, J.; Lengaigne, M.; Murty, V.S.N.; McPhaden, M.J. TropFlux: Air-sea fluxes for the global tropical oceans—description and evaluation. *Clim. Dyn.* **2011**, *38*, 1521–1543. [CrossRef]
78. Josey, S.A.; Pascal, R.W.; Taylor, P.K.; Yelland, M. A new formula for determining the atmospheric longwave flux at the ocean surface at mid-high latitudes. *J. Geophys. Res. Earth Surf.* **2003**, *108*, C4. [CrossRef]
79. Schiano, M.E.; Borghini, M.; Castellari, S.; Luttazzi, C. Climatic Features of the Mediterranean Sea Detected by the Analysis of the Longwave Radiative Bulk Formulae. *Ann. Geophys.* **2000**, *18*, 1482. [CrossRef]
80. Castellari, S.; Pinardi, N.; Leaman, K. A model study of air–sea interactions in the Mediterranean Sea. *J. Mar. Syst.* **1998**, *18*, 89–114. [CrossRef]
81. Bignami, F.; Marullo, S.; Santoleri, R.; Schiano, M.E. Longwave radiation budget in the Mediterranean Sea. *J. Geophys. Res. Earth Surf.* **1995**, *100*, 2501–2514. [CrossRef]
82. Gilman, C.; Garrett, C. Heat flux parameterizations for the Mediterranean Sea: The role of atmospheric aerosols and constraints from the water budget. *J. Geophys. Res. Earth Surf.* **1994**, *99*, 5119–5134. [CrossRef]
83. Nagy, H.; Lyons, K.; Nolan, G.; Cure, M.; Dabrowski, T. A Regional Operational Model for the North East Atlantic: Model Configuration and Validation. *J. Mar. Sci. Eng.* **2020**, *8*, 673. [CrossRef]
84. Hellerman, S.; Rosenstein, M. Normal Monthly Wind Stress Over the World Ocean with Error Estimates. *J. Phys. Oceanogr.* **1983**, *13*, 1093–1104. [CrossRef]
85. Noori, R.; Tian, F.; Berndtsson, R.; Abbasi, M.R.; Naseh, M.V.; Modabberi, A.; Soltani, A.; Kløve, B. Recent and future trends in sea surface temperature across the Persian Gulf and Gulf of Oman. *PLoS ONE* **2019**, *14*, e0212790. [CrossRef] [PubMed]
86. Nandkeolyar, N.; Raman, M.; Kiran, G.S.; Ajai. Comparative Analysis of Sea Surface Temperature Pattern in the Eastern and Western Gulfs of Arabian Sea and the Red Sea in Recent Past Using Satellite Data. *Int. J. Oceanogr.* **2013**, *2013*, 1–16. [CrossRef]
87. Tudhope, A.W.; Lea, D.W.; Shimmield, G.B.; Chilcott, C.P.; Head, S. Monsoon Climate and Arabian Sea Coastal Upwelling Recorded in Massive Corals from Southern Oman. *PALAIOS* **1996**, *11*, 347. [CrossRef]
88. Chaichitehrani, N.; Allahdadi, N. Overview of Wind Climatology for the Gulf of Oman and the Northern Arabian Sea. *Am. J. Fluid Dyn.* **2018**, *8*, 1–9.
89. Holbrook, N.J.; Scannell, H.A.; Gupta, A.S.; Benthuysen, J.A.; Feng, M.; Oliver, E.C.J.; Alexander, L.V.; Burrows, M.T.; Donat, M.G.; Hobday, A.J.; et al. A global assessment of marine heatwaves and their drivers. *Nat. Commun.* **2019**, *10*, 2624. [CrossRef]
90. Gupta, A.S.; Thomsen, M.; Benthuysen, J.A.; Hobday, A.J.; Oliver, E.; Alexander, L.V.; Burrows, M.T.; Donat, M.G.; Feng, M.; Holbrook, N.J.; et al. Drivers and impacts of the most extreme marine heatwave events. *Sci. Rep.* **2020**, *10*, 19359. [CrossRef]